Microfluidics and Nanofluidics (2025) 29:75
https://doi.org/10.1007/s10404-025-02842-3

RESEARCH

In the heart of a micro-mixer: characterisation of liquid-liquid flow hydrodynamics inside an advanced-flow micro-reactor

Filip Horvath-Gerber[1] · Surya Narayan[1] · Konstantin S. Pervunin[1] · Lyes Kahouadji[1] · Christian Holtze[2] · Eleonore J. C. Deublein[2] · Omar K. Matar[1] · Christos N. Markides[1] · Klaus Hellgardt[1]

Received: 27 April 2025 / Accepted: 20 August 2025
© The Author(s) 2025

Abstract
The hydrodynamic characteristics of liquid-liquid flows in a micro-mixing plate with a 'heart/spade' geometry and a hydraulic diameter of ~ 0.36 mm at the contraction point are studied experimentally in the Reynolds number range of $250 - 1,000$. Localised optical observations of the two-phase flow within the micro-mixing device units are performed using a high-speed camera in combination with an LED-induced fluorescence imaging technique. A qualitative interpretation of the instantaneous images enabled the development of a regime map with three stable flow patterns, each with a metastable transitional state. The formation of secondary flows and recirculation zones resulted in the breakup of interfaces and fragmentation of droplets. The droplet size distribution of an MTBE-water dispersion is studied across a broad range of the dispersed phase (water) ratios, $\phi_d = 0.091 - 0.714$. The resulting Sauter mean diameter of water droplets is used to evaluate the improvement in the specific surface area and was correlated as a function of the energy dissipation rate and the Reynolds and Weber numbers.

Keywords Micro-reactor · Liquid · Drop size · Interfacial area · High dispersed phase concentration

1 Introduction

In recent years, the utilisation of micro-reactor devices with characteristic lengths in the millimetre scale of the hydraulic diameter at the contraction point has garnered significant attention in the fine chemicals and pharmaceutical industries, offering versatile and efficient handling over harsh multi-phase processes (Mason et al. 2007; Hartman et al. 2011; Malet-Sanz and Susanne 2012; Hessel et al. 2013; Pastre et al. 2013). For these reasons, they have gained particular interest in process development and intensification of traditionally batch or semi-batch synthetic steps. In the instance of fast reactions taking place in a mass-transfer-limited multi-phase system (e.g., liquid-liquid processes), the rate of mass transfer within the reactor is dependent on the overall interfacial area of the given phases generated by the action of static mixing.

Of particular interest for fast homogeneous and heterogeneous reactions is the use of micro-mixing plate systems (Plouffe et al. 2014). These consist of identical two-dimensional static mixing units cascaded in series. A range of geometries have been developed and optimised for specific applications, with the 'heart/spade' geometry by Corning Advanced-Flow™ Reactors (AFR) (Corning 2016) and the 'LL' geometry by Lonza Ehrfeld FlowPlate® (Ehrfeld 2022) identified as the most suitable for the formation of liquid-liquid dispersions (Plouffe et al. 2016b).

Prior studies on the development and scale-up of liquid-liquid processes within mixing plates by Plouffe et al. (2016a, 2016b, 2016c) assessed the droplet size distribution and interfacial area in the drop flow regime through indirect experimental measurements of the overall mass transfer coefficient for alkaline hydrolysis of 4-nitrophenyl acetate. No direct measurements of droplet size distribution and interfacial area of dispersions formed within micro-mixing plates have been previously provided in the literature. Liquid-liquid dispersions in turbulent flows with the aim of predicting droplet sizes have been studied by many authors

✉ Filip Horvath-Gerber
fh3217@imperial.ac.uk

[1] Department of Chemical Engineering, Imperial College London, South Kensington Campus, SW7 2AZ London, UK

[2] BASF SE, 67063 Ludwigshafen am Rhein, Germany

Published online: 09 October 2025

in the past, utilising mainly the Kenics mixer (Middleman 1974; Lemenand et al. 2003; Yamamoto et al. 2007) and the Sulzer mixer designs (SMV, SMX, SMXL,...) (Streiff et al. 1997; Hirschberg et al. 2009; Theron et al. 2010; Theron and Sauze 2011; Lobry et al. 2011). While the majority of these studies have been performed with dispersed phase ratios, $\phi_{\mathrm{d}} \leq 0.25$, only a few have dealt with a broader range of phase fractions and their effect on the droplet size distribution.

It is beneficial to contrast experimental values of droplet size distribution with well-established correlations. The commonly referenced theory of turbulent dispersion is based on the classical theory of turbulence developed by Kolmogorov (1949) and Hinze (1955) to predict droplet sizes depending on the energy dissipation rate generated by the static mixers. Dimensionless form of this correlation was derived by Middleman (1974) and experimentally validated for turbulent dispersions in Kenics mixers (Middleman 1974). As the theory was initially developed for mixing in turbulent regime, few authors have worked to address liquid-liquid dispersions under laminar and transient flow conditions, where the drop deformation is due to shearing deformation stresses and vortex stretching (Das et al. 2005).

In recent times, the management of continuous and batch processes has increased in importance. The accurate control of the mean droplet diameter and size distribution for assessment of the interfacial area between liquid phases is one of the main parameters, as enhanced mixing performance is hailed as a key benefit in the use of micro-mixing plates. As both 'heart/spade' and 'LL' geometries were designed uniquely for the application of heterogeneous liquid-liquid processing, direct or *in situ* measurement of these parameters is desirable. This can provide further insight into the overall mass-transfer coefficient for a mass-transfer-limited reaction.

For direct measurements and control of droplet size distribution within the operating system, several on-line analytical techniques have been developed in addition to the classical off-line sampling ones. These measurement techniques are characterised as either direct *in situ* measurements (e.g., laser-induced fluorescence, video microscopy) or *ex situ* measurements at the outlet of the mixing unit (e.g., light back-scattering turbiscan), in which surfactants are commonly added to stabilise developed droplets from coalescing. A comparison of these techniques with all their corresponding advantages and drawbacks was discussed extensively by Lobry et al. (2011). In this direction, a high-speed imaging technique for the accurate identification of phases in a liquid-liquid mixing plate with *in situ* quantification capabilities of the droplet size distribution for a broad range of dispersed phase ratios could be immensely beneficial. Furthermore, imaging techniques could additionally provide insights into the evolution of the flow regime within individual units of the micro-mixing system enabling optimal scaling of the reactor design.

To this end, the purpose of this study is to provide *in situ* measurement of hydrodynamically-controlled droplet size distribution within an in-house constructed 'heart/spade' micro-mixing plate using a light-emitting diode (LED)-induced fluorescence imaging technique. The experiments were performed by discretely adjusting the individual flow rates of two immiscible fluids, namely deionised water and Methyl tert-butyl ether (MTBE) seeded with Pyrromethane-567 (PM-567), from 0.5 mL/min to 5.0 mL/min to achieve a broad range of dispersed phase ratios, $\phi_{\mathrm{d}} = 0.091 - 0.714$ in a laminar to transient flow regime of the Reynolds numbers $250 - 1,000$. The observations of the flow pattern evolution in the initial micro-mixing units have been validated by computational fluid dynamics simulation and the underlying mechanisms were expanded upon.

Following this, a statistical representation of the droplet size distribution was obtained through post-processing of a selected set of instantaneous images to estimate the key droplet sizing parameters, including the Sauter mean droplet diameter, d_{32}. The evaluated values of Sauter mean droplet diameters were contrasted with the well-established Hinze-Kolmogorov correlation for energy dissipation rates and the Middleman's dimensionless correlation together with its alternatives for laminar and transient flow conditions.

2 Experiment and simulation

2.1 Experimental facility and optical configuration

The micro-mixing equipment was designed based on the 'heart/spade' geometry within Corning Advanced-Flow$^{\mathrm{TM}}$ Reactor with channel sizing corresponding to the Low Flow module (Fig. 1) (Corning 2016). Mixing channels were milled out of Stainless Steel 316 (SS316) plate using a computer numerical control (CNC) machine to a depth of ~ 0.36 mm, see Fig. 2. The width of the channel at the contraction point was designed to be ~ 0.36 mm, resulting in the hydraulic diameter of the nozzle, $d_{\mathrm{h}} \approx 0.36$ mm. The micro-reactor employed in the present study was made up of 31 identical micro-mixer units (shown in Fig. 2) cascaded in series with a total internal volume, V_{R}, of ~ 0.228 cm^3.

Experiments were performed using an immiscible liquid-liquid mixture of MTBE (99%, pure, Thermo Scientific Chemicals) and deionised water, with their physical properties of density, ρ, viscosity, μ, and associated interfacial tension, σ, specified in Table 1. MTBE and water were pumped into the micro-mixing system at pre-determined flow rates using dedicated calibrated Jasco PU-1580 Intelligent HPLC pumps for each fluid. The pressure drop across a series of

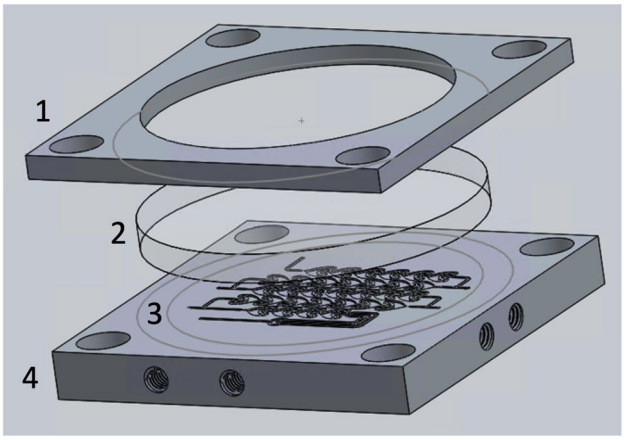


Fig. 1 Composition of the experimental 'heart/spade' micro-mixing plate manufactured in close accordance with the geometry of a Corning Advanced-Flow^{TM} Reactors (AFR) Low Flow micro-reactor: 1 - top cover plate, 2 - quartz glass, 3 - FEP sealing foil, 4 - bottom plate with embedded micro-channels

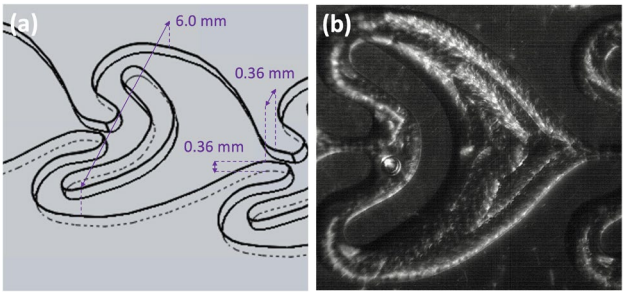


Fig. 2 Design of the 'heart/spade' micro-mixing units: (**a**) 3D isometric view of an individual micro-mixing unit with an indication of its dimensions, and (**b**) top-view photograph of the manufactured channel

Table 1 Physical and thermodynamic properties of the working liquids at standard temperature (20 °C) and pressure (1 bar) conditions

Solvent	σ (mN/m)	ρ (kg/m^3)	μ (Pa s)
MTBE	9.298	745.189	3.454 x 10^{-4}
Water	-	990.078	1.002 x 10^{-3}

micro-mixing units (i.e., 4, 11, 18, 25, 31 in number, dictated by the design of the mixing plate) was measured using Labom PASCAL CS2110 pressure transmitters. The inlet temperature was monitored using a *K*-type insulated thermocouple. The temperature and pressure were monitored and logged into a file at a rate of 1 datapoint per second using an OMEGA DAQ USB-2400 series system.

The fluorescence technique used in the present research is an extension of laser-induced fluorescent (LIF) measurement approaches the authors used in previous studies of immiscible liquid-liquid flows (Morgan et al. 2013; Ibarra et al. 2018). Here, Pyrromethane-567 (CAS: 131083-16-4, Mw = 318.21 g/mol), a hydrophobic fluorescent dye, at a concentration of 1.57 μmol/dm^3 was employed as a fluorophore and was uniformly dispersed into MTBE. A blue light-emitting diode (LEDs) array with a total power of 54 W and a peak irradiance at the wavelength of 460 nm (full-width half maximum (FWHM) = 10 nm) was used as an excitation source for the fluorophore. The fluorescent dye absorbs a portion of light from the LED array and emits longer wavelengths between $\sim$ 540 nm and $\sim$ 575 nm with a characteristic peak at $\sim$ 560 nm.

The test section is optically accessible from only one side, therefore, illumination and video recording were implemented through the same port which was made from a 6 mm thick fused quartz window equipped with a $\sim$ 200 μm thin transparent fluorinated ethylene propylene (FEP) foil that acted as a transparent sealing gasket sandwiched between the quartz window and SS316 micro-reactor (Wright et al. 2017). The fluorescence emission was registered using a CMOS Phantom VEO-310L high-speed camera (digit capacity = 12 bit, full resolution = 1,280 $\times$ 800 pixels, maximum recording rate = 3200 fps at full resolution, minimum exposure = 1 μs) at full resolution with an exposure of 50 μs and recording rate of 100 Hz, fitted with a Sigma 105 mm f/2.8 EX DG Macro lens in combination with a 36 mm extension ring and a long-pass filter with cutoff edge at 560 nm to selectively register the fluorescence emission of the dye. The optical magnification and spatial resolution of this configuration of the imaging system schematically shown in Fig. 3 was $\sim 2\times$ and $\sim$ 10 μm/pixel, respectively.

The static contact angle of MTBE and DI water on an unpolished SS316 surface was measured to be $\sim$ 17° and $\sim$ 34°, respectively, using a goniometer. MTBE with the lower contact angle and, thus higher surface wettability, compared to DI water, represents the continuous phase, an aspect that finds support through visual observation in Fig. 7.

2.2 Data processing and analysis

Each experimental run involved the recording of sequences of background images, with only MTBE seeded with the fluorescent dye circulated through the micro-mixer plate (Fig. 4a), and test images, where both water and MTBE flow through the micro-mixer at pre-determined flow rates (Fig. 4b). The time-lapse background image sequence consisting of 1,000 individual snapshots was averaged and binarised using an intensity threshold determined by the Otsu method (Otsu 1979) to distinguish the metallic walls of the micro-mixer from the region occupied by MTBE, see Fig. 4c.

This binarised picture was then overlayed onto the test image sequence and the background intensity distribution. Using the information on the local intensity of the average background image, a procedure of adaptive segmentation was applied to indicate regions occupied by the dispersed phase (water droplets) as 1, while keeping areas occupied by both metallic walls and MTBE (continuous phase) as 0.

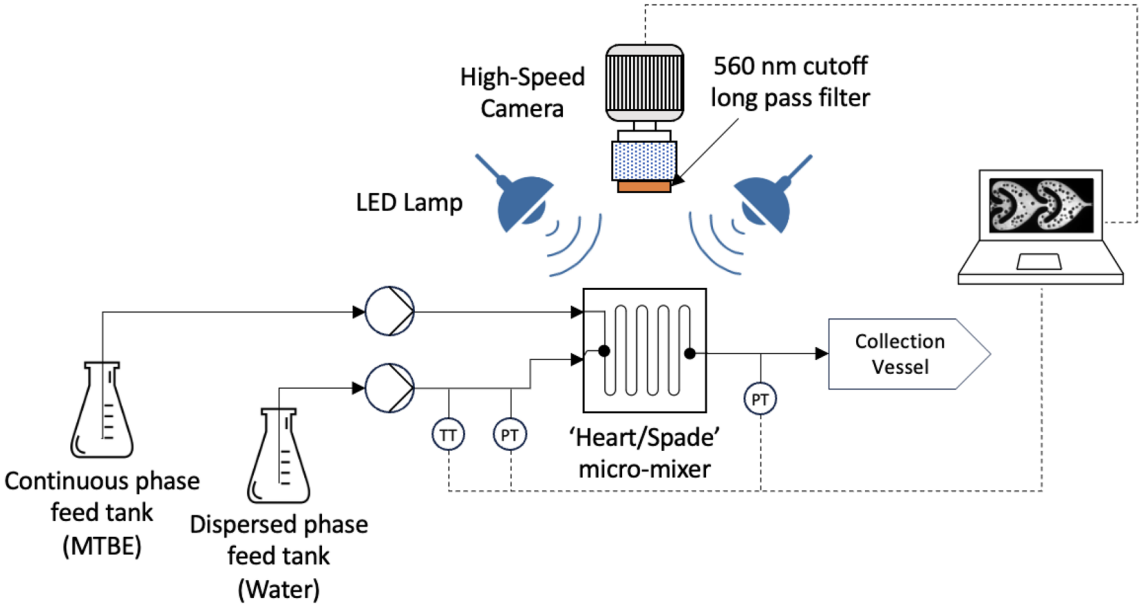


Fig. 3 Flow diagram of the experimental apparatus displaying the relative arrangement of the visualisation system. TT and PT indicate the temperature and the pressure transmitters respectively

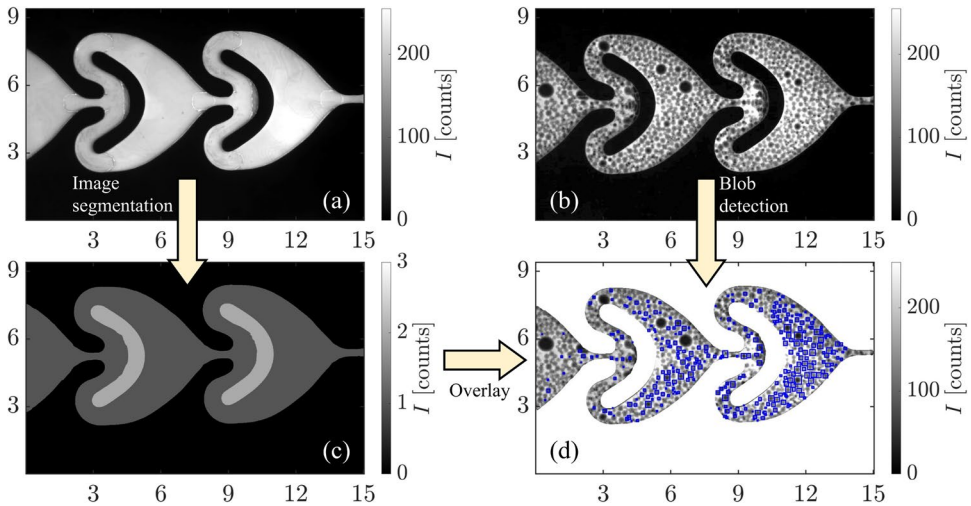


Fig. 4 Flowchart describing the image processing steps. (**a**) Reference background image with the test channel completely filled with dye-seeded MTBE, (**b**) representative experimental image at the dispersed phase ratio $\phi_{\mathrm{d}} = 0.5$ and the flow rates of the continuous $Q_{\mathrm{MTBE}} = 2.5$ mL/min and dispersed phase $Q_{\mathrm{water}} = 2.5$ mL/min, (**c**) Segmented regions of the reference image, (**d**) Identified blobs along with their corresponding bounding box (blue rectangles) to display each detected droplet

Meanwhile, the image scale factor was estimated by calculating the number of pixels covering the maximum width of each micro-mixing unit which was known beforehand to be $\sim$ 6 mm. In the present study, the spatial scale of the recorded images was $\sim$ 10 μm/pixel.

Using the watershed transform on the final binarised picture, where the regions occupied by droplets were indicated by 1, connected (i.e., in contact) blobs were separated from each other. Following this, a drop detection methodology, as described in the image processing toolbox of MATLAB, was employed to quantify their sizes in all experimental conditions. An eccentricity ($0.9 \leq e \leq 1.2$) and size-based filter ($10\ \mu\mathrm{m} \leq D \leq 0.40$ mm), were applied depending on the experimental conditions to remove spurious detections of the droplets. After their identification, a bounding box was overlayed on each droplet, see Fig. 4d.

The above steps of image post-processing were repeated for randomly selected unbiased samples of 100 consecutive snapshots of the 30^{th} and 31^{st} micro-mixing units in all flow regimes. The data on blob equivalent diameters extracted from each image were collected together to reconstruct a droplet size distribution. For a given size range (d_i) in the histogram with a bin width of $\sim$ 10 μm and the corresponding number of detections in each bin (n_i), the Sauter mean droplet diameter, d_{32}, was estimated through:

$$d_{32} = \frac{\sum_{i=1}^{n} n_i d_i^3}{\sum_{i=1}^{n} n_i d_i^2} \tag{1}$$

Apart from this, diameters corresponding to 10%, 50% and 90% of the cumulative probability distribution function (CPDF) obtained by summing up the probabilities of individual bins in Fig. 5, were evaluated to calculate the span of the histogram through:

$$\Delta_{\mathrm{S}} = \frac{d_{90} - d_{10}}{d_{50}} \tag{2}$$

In the present study, the dispersed phase ratio, ϕ_{d}, is defined with respect to the total volume flow rate, Q_{tot}, by relating individual flow rates of the given phases as:

$$\phi_{\mathrm{d}} = \frac{Q_{\mathrm{d}}}{Q_{\mathrm{c}} + Q_{\mathrm{d}}} = \frac{Q_{\mathrm{d}}}{Q_{\mathrm{tot}}} \tag{3}$$

where Q_{c} and Q_{d} denote the flow rates of the continuous and dispersed phases, respectively.

2.3 Errors and uncertainty

Errors in setting-up of the governing integral parameters determining the flow regime can be related to the measurement of the flow rate, fluid temperature and pressure drop across the experimental apparatus. In the experiment, we employed K-type thermocouples, native to the OMEGA DAQ system without the need for calibration, to an accuracy of ± 1.5 °C. The pump flow rates were calibrated by repeated volume-over-time measurements using a beaker to an accuracy of ± 0.05 mL/min. Each pressure transducer had an accuracy of ± 2 mbar. The maximum uncertainty in the pressure drop was found to be ≈ 4.4%. Uncertainty of the estimation of the equivalent diameter is mostly related to the blob-detection algorithm. For 90% confidence in the droplet identification, the binary image region occupied by a blob should be at least 5 pixels in size, which corresponds to $\sim$ 50 μm. The estimation of the d_{32} involves statistical analysis of several instantaneous images, and as a result, the average variance in the value of d_{32} is given by its two-standard deviation values which is found to be $< 13\%$, with the maximum variance $< 35\%$ under conditions associated with high Δ_{S}.

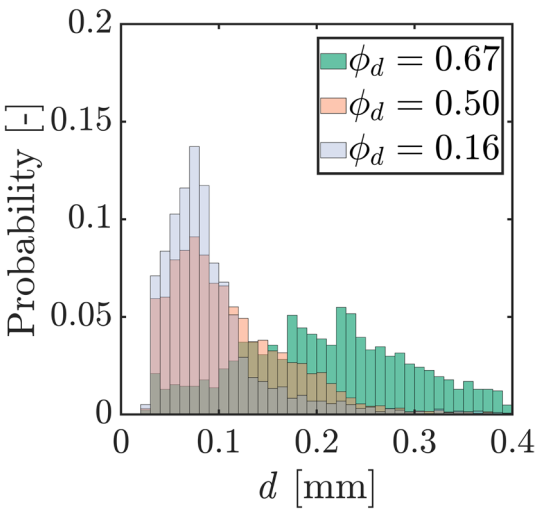


Fig. 5 Dependence of the probability distribution function for droplets found in 100 successive images for the dispersed phase ratios ϕ_{d} = 0.16, 0.50 and 0.67 at the flow rate of the continuous phase Q_{MTBE} = 2.5 mL/min. The bin width in the histogram is equal to ≈ 10 μm which corresponds to a digital scale of 1 pixel

2.4 Numerical method

The mathematical model for the two-phase flow inside the microfluidic 'heart/spade' micro-mixer, illustrated in Fig. 2, consists of solving the full set of the Navier-Stokes equations in a three-dimensional domain $\mathrm{x} = (x, y, z) \in [0, 19.125] \times [0, 6.12] \times [0, 0.37]$ mm^3. The governing equations for the transport of an incompressible two-phase flow are:

$$\begin{gathered} \nabla \cdot \mathrm{u} = 0 \\ \rho\left(\frac{\partial \mathrm{u}}{\partial t} + \mathrm{u} \cdot \nabla \mathrm{u}\right) = -\nabla p + \nabla \cdot \mu\left(\nabla \mathrm{u} + \nabla \mathrm{u}^{\mathrm{T}}\right) + \mathrm{F} \end{gathered} \tag{4}$$

Here, u is the velocity, p is the pressure, and F is the local surface tension force at the interface. The physical properties of both phases, such as density and viscosity, are defined in the entire domain using a spatio-temporal function $\mathcal{H}(x, t)$ considered zero and unity in the continuous and dispersed phase, respectively:

$$\begin{aligned} \rho(\mathrm{x}, t) &= \rho_{\mathrm{c}} + (\rho_{\mathrm{d}} - \rho_{\mathrm{c}})\,\mathcal{H}(\mathrm{x}, t) \\ \mu(\mathrm{x}, t) &= \mu_{\mathrm{c}} + (\mu_{\mathrm{d}} - \mu_{\mathrm{c}})\,\mathcal{H}(\mathrm{x}, t) \end{aligned} \tag{5}$$

where the subscripts c and d stand for the continuous (MTBE) and dispersed (water) phase, respectively (see Table 1).

The construction of the 'heart/spade' shape follows the same approach as in Kahouadji et al. (2018) and Kalli et al. (2023), where a static distance function is used. The function is positive for the fluid domain, which includes both phases and negative for the solid wall. Finally, the contour shown in Fig. 6 represents a zero iso-contour of the static distance function. The Navier-Stokes equations (4) are solved by the classic projection method by Chorin (1968), where temporal discretisation follows the second-order Gear scheme by Wang and Wen (2006). The computational domain is discretised with a uniform fixed 3-D finite-difference mesh ($1600 \times 512 \times 32$) following the procedure of standard staggered MAC cell arrangement by Harlow and Welch (1965). All three components of the velocity field u

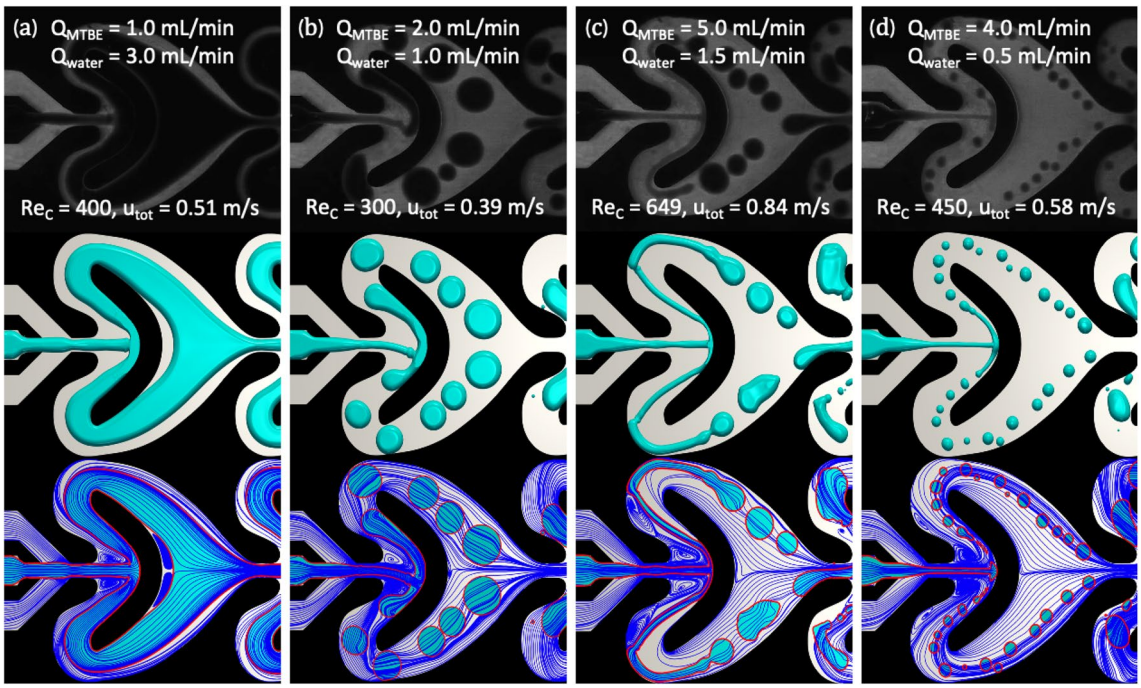


Fig. 6 Flow pattern modification within the initial unit of the 'heart/spade' micro-mixer with changes in the flow conditions specified in the experimental snapshots (upper row). The photographs are placed next to the calculated contours of the dispersed phase (middle row). The lower row shows the flow streamlines obtained by CFD for each regime to highlight the formation of both secondary flows and vortices/eddies

are defined on the corresponding cell faces while the pressure field p, considered here as a scalar variable, is located at the cell centres, and all spatial derivatives are approximated by second-order central differences. Finally, the treatment of the interface relies on our high-fidelity hybrid front-tracking/level-set method, which uses a Lagrangian triangle interface mesh. We refer readers to Shin et al. (2017, 2018) for more details, where the interfacial force F in eq. (4) is also defined.

3 Results and discussion

3.1 Flow patterns and regime map

The evolution of the flow pattern was observed experimentally within the initial units of the 'heart/spade' micro-mixer. The CFD simulation, outlined in Section 2.4, was performed using the fluid properties given in Table 1 and dimensions of the micro-mixer. The visual observations were compared with the results of the CFD analysis demonstrating good agreement in terms of tracing the flow pattern evolution as shown in Fig. 6. The CFD simulation also enabled the visualisation of secondary flow patterns and vortices/eddies formed as a result of jetting of the dispersed phase through the nozzle and its subsequent hit at the concave front surface of the C-shaped static barrier.

For the stable and transitional parallel flow regimes in the region of $Q_{\mathrm{MTBE}} \leq 1.5$ mL/min and $Q_{\mathrm{Water}} \geq 3$ mL/min, the core region of the micro-mixing units was occupied by water while MTBE was predominantly distributed at the periphery of the channel and in the stagnation zone behind the centrally-located C-shaped static barrier, shown in Fig. 6a. This parallel pattern was observed throughout the micro-mixer apparatus with the purely laminar nature of the fluid motion featured by recirculation zones produced behind the C-shaped barrier and nozzle walls (see Fig. 6a).

At low flow rates of both Q_{water} & $Q_{\mathrm{MTBE}} \leq 2$ mL/min, the core region in the parallel flow was broken up into moderate sized droplets, thereby resulting in the establishment of the slug flow pattern (Fig. 6b). The oscillatory behaviour of the dispersed phase jet is detected before hitting the C-shaped barrier as a consequence of the development of an asymmetric Plateau–Rayleigh instability, visually observed in the form of capillary pinching. The oscillatory behaviour is contrary to the cases seen in Fig. 6c and 6d, and resembles the flow dynamic commonly observed in fluidic oscillators.

Increasing both Q_{water} and Q_{MTBE} makes the dispersed phase jet take a purely cylindrical shape, as seen in Fig. 6c. The capillary pinching effect begins to manifest itself only far downstream, after passing the C-shaped barrier, where an increase in the cross-sectional area results in a decrease of the mixture velocity. When the ratio of Q_{MTBE} to Q_{water} is increased at a higher total flow rate, the continuous phase

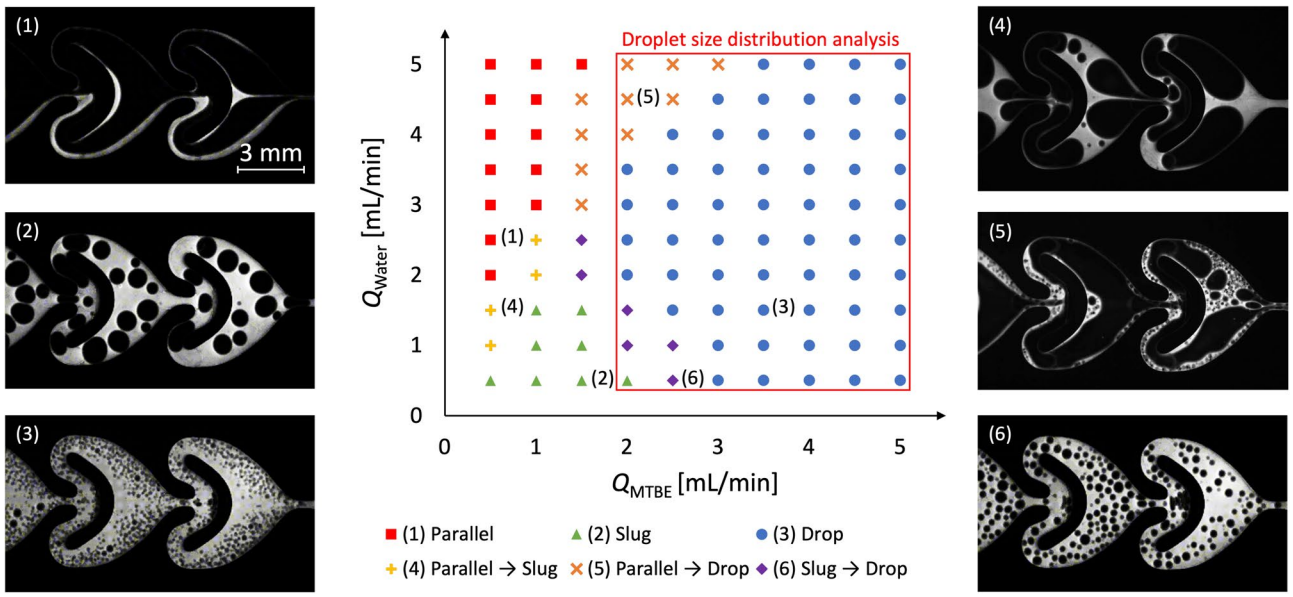


Fig. 7 Flow regime map of the MTBE-Water mixture in the 'heart/spade' micro-mixers visualised within the 30^{th} and 31^{st} micro-mixing units

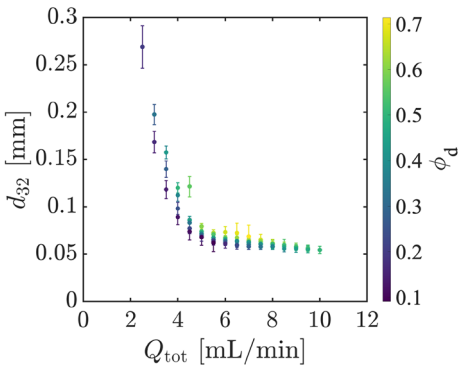


Fig. 8 Dependence of the Sauter mean diameter, d_{32}, of water droplets on the total flow rate, Q_{tot}, at a range of the dispersed phase ratio, ϕ_{d}

shears the dispersed phase through the contraction point thanks to the mechanism of Kelvin-Helmholtz instability. Thus, the drop flow regime is established in the initial micro-mixer unit as a result of the effects of shearing and capillary pinching, shown in Fig. 6d.

Visual observations at each flow rate within the final 30^{th} and 31^{st} micro-mixing units involved recording a sequence of images that enabled classification of the developed flow patterns into six distinctive regimes which include three stable states: (a) parallel, (b) slug, and (c) drop flow along with corresponding metastable transitional regimes in between. By identifying the flow patterns for each experimental condition, a regime map was eventually constructed as shown in Fig. 7. A representative image for each developed stable and transitory flow pattern was provided for visual identification.

3.2 Effect of total flow rate on in situ droplet size measurements

The statistical analysis of droplet sizes was carried out by post-processing a randomly selected set of 100 images for $Q_{\mathrm{MTBE}} \geq 2$ mL/min, which corresponded to a broad range of the dispersed phase ratios, ϕ_{d}, from 0.091 to 0.714. Moreover, for the same flow conditions, increasing the total flow rate ($Q_{\mathrm{tot}} = Q_{\mathrm{MTBE}} + Q_{\mathrm{water}}$) led to a rapid decrease in the expected values of the Sauter mean diameter, d_{32}, starting from ~ 270 μm and asymptotically converging to the minimum quantifiable diameter of ~ 50 μm covering an image region of ≈ 5 pixels, see Fig. 8.

The plausible reasons for the asymptotic plateau of d_{32} at high total flow rates can be attributed to the total kinematic energy of the flow available for the vortex-induced breakup of the interface between the phases, an aspect that forms the basis of discussion in Section 3.3.

The histogram span, Δ_{S}, expressed by Eq. 2, is a measure of droplet size distribution uniformity. For example, when Δ_{S} is closer to zero, the droplet size distribution is more uniform and the size consistency is high. When $\Delta_{\mathrm{S}} = 1$, the droplet size distribution is symmetrical. Δ_{S} is visualised with respect to Q_{tot} in Fig. 9. While the majority of the evaluated Δ_{S} fall within the higher uniformity in the range of $1.1 - 1.6$, a lower uniformity of the droplet size distribution with $\Delta_{\mathrm{S}} > 1.6$ is visible at higher dispersed phase ratios, $\phi_{\mathrm{d}} > 0.6$, which is associated with the transitional parallel $\rightarrow$ drop flow pattern, as shown in Fig. 7. These observations of the Δ_{S} behaviour with Q_{tot} match the prior findings by Lobry et al. (2011).

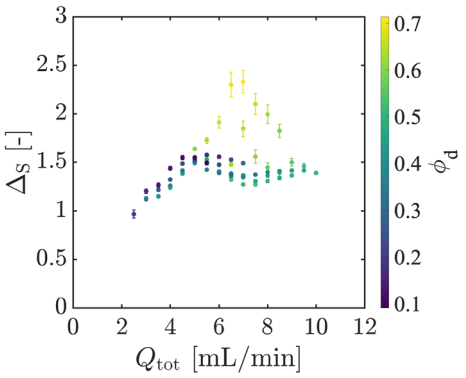


Fig. 9 Dependence of the droplet size distribution histogram span, Δ_S, on the total flow rate, Q_{tot}, at a range of the dispersed phase ratio, ϕ_d

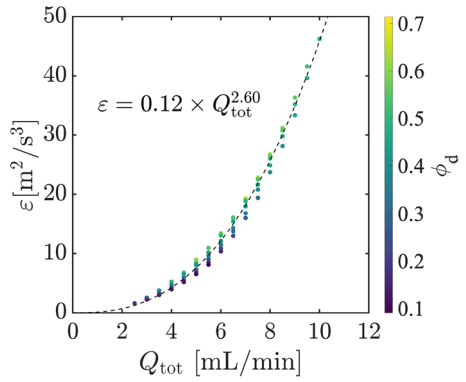


Fig. 10 Energy dissipation rate, ε, as a function of the total flow rate, Q_{tot}, at a range of the dispersed phase ratio, ϕ_d

3.3 Role of energy dissipation in breakup of liquid interface

Within the investigated micro-mixer system, the Reynolds number of the continuous phase is defined using the total mixture velocity at the contraction point, u_{tot}, density of the continuous phase, ρ_c, and its dynamic viscosity, μ_c, as follows:

$$\mathrm{Re}_c = \frac{\rho_c d_h u_{tot}}{\mu_c}, \tag{6}$$

which ranged from 100 to 1,000. Under these conditions, the two-phase flow was laminar. However, the presence of the 'heart/spade' geometry in the micro-mixing channel, designed specifically to aid in the formation of recirculation zones that enable the mixing, resulted in shearing of the water droplet (dispersed phase) interface, leading to its disruption followed by the formation of numerous smaller droplets at increased Q_{tot}, as seen from Fig. 8. It is important to note that all the values of d_{32} shown in Fig. 8 correspond to the flow rate range of $2.0 - 5.0$ mL/min of MTBE (organic continuous phase) and, as a result, the reduced range of $\mathrm{Re}_c = 250 - 1,000$. Additionally, a plateau in Sauter mean diameter, d_{32}, is observed upon increasing the total flow rate, Q_{tot}, in Fig. 8 and increasing the energy dissipation rate, ε, in Fig. 11, indication the camera system reaching its spacial resolution of ~ 10 μm/pixel, as outlined in Section 2.1.

In order to deeper understand the role of the mechanism of vortex-induced droplet breakup, the total energy dissipation rate, ε, was related to Q_{tot} of the micro-mixer system and the measured cumulative pressure drop, ΔP, across a set reactor volume, V_R:

$$\varepsilon = \frac{\Delta P Q_{tot}}{\rho_c V_R} \tag{7}$$

In the present study, ΔP in the micro-mixer system was measured using two pressure transducers across a total of 31 micro-mixing units, as indicated in Fig. 3.

The total energy dissipation rate is directly related to the size, frequency and kinetic energy of vortices formed by the C-shaped physical barrier. These vortices must cause shear deformation of the liquid-liquid interface. Perturbations induced by the vortices at the phase boundaries resulted in droplet breakup into smaller-sized blobs at higher total flow rates, which finds support in the form of the d_{32} decline shown in Fig. 8. This reduction in the droplet size at high Q_{tot} led to a rapid growth of ΔP across each micro-mixing unit resulting in an overall increase in ε, as seen in Fig. 10.

The Hinze-Kolmogorov theory (Hinze 1955; Kolmogorov 1949) postulates that the energy contained in large-scale vortices is progressively transferred without dissipation to smaller length-scale vortices within the inertial and viscous (dissipation) ranges until a minimum vortex size is reached, commonly termed as 'Komologorov length scale', l_k, which can be estimated through:

$$l_k = \left(\frac{\mu_c^3}{\rho_c^3 \varepsilon}\right)^{0.25} \tag{8}$$

Vortical structures/eddies smaller than this length-scale cannot exist as their kinetic energy is quickly dissipated to heat due to the viscous effects and, therefore, cannot contribute to the interface breakup. Hence, the fragmentation of droplets down to l_k requires a significant increase in ε (seen evidently in Fig. 11), which can subsequently lead to a larger pressure drop. In the present study, d_{32} values for all experimental conditions were estimated to be at least an order of magnitude higher than l_k defined by Eq. 8, as visible in Fig. 11.

The graph in Fig. 11 suggests that, by increasing the number of the micro-mixing units above 31, it may hypothetically be possible to reduce the size of the droplets down

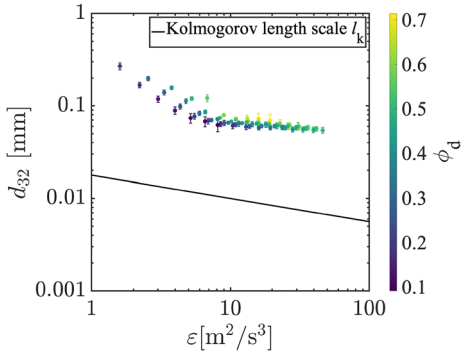


Fig. 11 The Sauter mean diameter of droplets, d_{32}, and the Kolmogorov length scale, l_k, against the total energy dissipation rate, ε, at a range of the dispersed phase ratio, ϕ_d

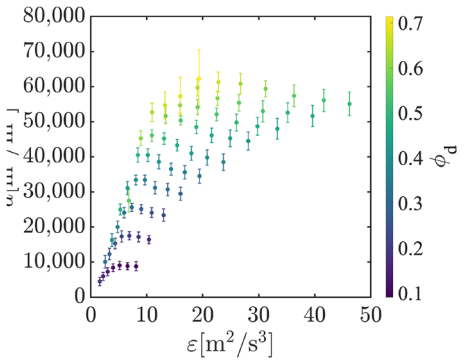


Fig. 12 Specific interfacial area, a, in the drop flow conditions as a function of the total energy dissipation rate, ε, at a range of the dispersed phase ratio, ϕ_d

to the theoretical limit given by l_k. However, increasing the total number of the micro-mixing units would lead to a significant increase in the total pressure drop, which might affect the scalability of this micro-mixer design and forms the scope of future studies.

Using the definition of d_{32}, the specific interfacial area, a, in a fully-developed drop flow regime can be related to ϕ_d through:

$$a = \phi_d \frac{6}{d_{32}} \tag{9}$$

As d_{32} and ε have complementary trends with Q_{tot}, a was found to increase significantly, by nearly 14 times as ϕ_d grows from 0.091 to 0.714 and ε rises from $\sim$ 16 to $\sim$ 193 m^2/s^3, as seen in Fig. 12.

Increased a is highly beneficial for the performance of a mass transfer limited chemical reaction in any micro-mixing continuous flow reactor. It is easier to comprehend this aspect through the fundamental relation for the overall mass transfer coefficient, $K_{org}a$, given by:

$$K_{org}a = -\frac{\phi_{org}}{\tau} \ln(1-\eta), \tag{10}$$

where τ is a micro-mixer residence time at a given flow rate, ϕ_{org} is an assumed organic phase ratio with a dissolved substrate and η is a performance indicator stated as chemical reaction conversion. The latter is strongly dependent on a nested within the $K_{org}a$ group. Thus, an increase in a can provide a significant improvement in the total yield of mass transfer limited chemical reactions.

Note that this experimental research was performed specifically to understand the hydrodynamics of various flow regimes taking place inside the present micro-mixing system. Hence, further discussion related to the performance of chemical reactions and improvements to K_{org} is beyond the scope of this study.

3.4 Prediction of droplet diameter

Many correlations have been proposed in the literature over the years to predict the droplet size from dispersion in static mixers, as summarised by Lobry et al. (2011). It is important to note that the majority of these empirical correlations are based on the Hinze-Kormologov theory (Kolmogorov 1949; Hinze 1955), which assumes a homogeneous and isotropic turbulence flow field. These formulations enable the prediction of the maximum stable droplet size, d_{max}, at a given energy dissipation rate, ε, and the correlations observed by different authors vary in the value of a proportionality constant, K. A detailed evaluation of the maximum droplet size capable of withstanding the turbulent stress forces based on the Hinze-Kolmogorov fundamental theory is provided in Appendix. In general, the mathematical formulation of d_{max} through the available empirical correlations based on ε within the micro-mixing system can be expressed as:

$$d_{max} = K \left(\frac{\sigma}{\rho_c}\right)^{0.6} \varepsilon^{-0.4} \tag{11}$$

A generalised proportionality between d_{max} and d_{32}, independent of the flow environment and conditions, was proposed by Lemenand et al. (2003). Due to the simplicity of its measurement, d_{90} corresponding to 90% of CPDF (see Section 2.2) is commonly used instead of d_{max}. The two-fold proportionality, as outlined by Lemenand et al. (2003), is:

$$d_{max} \approx d_{90} \approx 2d_{32} \tag{12}$$

The present study provides a visualisation of the proportionality between d_{32} and d_{90} in Fig. 13. The deviation from the expected proportionality is significant for $\phi_d \geq 0.6$, as it was also indicated in the span analysis in Fig. 9, which

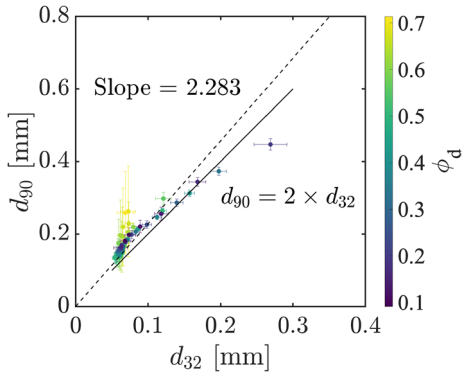


Fig. 13 Proportionality of the maximum droplet diameter characterised by d_{90} to the Sauter mean diameter of droplets, d_{32}, at a range of the dispersed phase ratio, ϕ_d. The solid line corresponds to $d_{90} = 2 \times d_{32}$ and the dashed line to the actual slope of linear fit forced through the origin

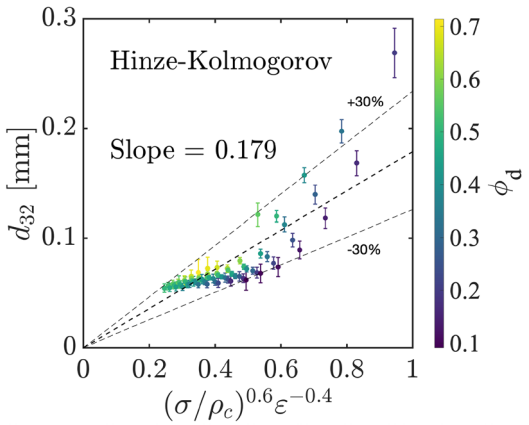


Fig. 14 Dependence of the Sauter mean diameter of droplets, d_{32}, on the total energy dissipation rate, ε, according to the model developed from the Hinze-Kolmogorov theory of turbulence (Eq. 13) at a range of the dispersed phase ratio, ϕ_d

corresponds to the transitional parallel → drop flow regime. It is important to note that both d_{32} and d_{90} were quantified through *in situ* measurements, and therefore, directly represent the hydrodynamic breakup of droplets without adding surfactants to limit their coalescence. By combining Eq. 11 and Eq. 12, the modified prediction model for d_{32} with experimentally observed values of ε can be written as:

$$d_{32} = \frac{1}{2} K \left(\frac{\sigma}{\rho_c} \right)^{0.6} \varepsilon^{-0.4} \tag{13}$$

Several prior studies of liquid-liquid dispersions have shown good prediction capability for d_{max} based on ε. The empirical constant was shown to be system-dependent with slight discrepancies, with the reported values of K equalled 0.725 by Hinze (1955), 0.940 by Streiff et al. (1997), $0.770 - 0.892$ by Lobry et al. (2011) and 0.718 by Plouffe et al. (2016c). In our study, the estimated K value is approximately 0.358 ($K_2 = 0.179$), showing a large deviation from prior findings. Prior experimental studies differ from current analysis by previously stabilizing droplets formed in a turbulent flow regime using a surfactant and evaluating d_{32} at the outlet of the static mixer.

In our study, it was estimated to be $K \approx 0.898$, which is in line with the earlier findings by the other researchers. The outcome of the model given by Eq. 13 yielded a root-mean-square error (RMSE) of 10.2% to the observed values of d_{32}, illustrated in Fig. 14.

A non-dimensional approach based on the Hinze-Kolmogorov model to estimate d_{32} was first derived and experimentally validated by Middleman using the Weber and Reynolds numbers for the continuous phase (Middleman 1974). For this, data from dispersions formed in Kenics static mixers under turbulent flow conditions (Re >3,000) with a characteristic channel diameter, D, was used. The functional form of this non-dimensional model is:

$$\frac{d_{32}}{D} = K \mathrm{We}_c^{-0.6} f^{-0.4}, \tag{14}$$

where f is the Fanning friction factor (Al Taweel and Walker 1983; Lobry et al. 2011). It is important to note that the Reynolds number of the continuous phase under turbulent flow conditions, $\mathrm{Re}_c > 2,300$, has a Blasius-like dependence on the Fanning friction factor, i.e., $f \propto \mathrm{Re}^{-1/4}$ (Streiff et al. 1997; Bird et al. 1960). Thus, in the present study, the model for estimation of d_{32} in the micro-mixer channel is associated with the hydraulic diameter at the contraction point ($d_h \approx 360\ \mu$m) as follows:

$$\frac{d_{32}}{d_h} = K \mathrm{We}_c^{-0.6} \mathrm{Re}_c^{0.1} \tag{15}$$

The proportionality constant, K, was shown by Matsumura et al. (1981) to be dependent on the viscosity of the emulsion, leading to the introduction of physico-chemical parameters into the correlation, for example, the viscosity ratio by Haas (1987). After Middleman (1974), a similar correlation was developed for Sulzer mixers (SMV, SMX, SMXL) by Streiff et al. (1997), followed by correlations assuming that the flow through static mixers is analogous to that through porous media by Legrand et al. (2001), and considering the impact of shear rate by Das et al. (2005). The developed correlations are listed in Table 2.

According to Legrand et al. (2001), in a flow through porous media, the Reynolds and Weber numbers are expressed as follows:

$$\mathrm{Re}_p = \frac{\rho_e d_p u_{tot}}{\mu_c} \tag{16}$$

Table 2 Models developed to correlate the mean droplet diameter of dispersions formed within static mixers

Authors	Static mixer	Correlation	Flow type	K	RMSE
Middleman (1974)	Kenics	$\frac{d_{32}}{D} = K\mathrm{We}_\mathrm{c}^{-0.6}\mathrm{Re}_\mathrm{c}^{0.1}$	Turbulent	0.592	16%
Streiff (1977)	SMV	$\frac{d_{32}}{D} = 0.21\mathrm{We}_\mathrm{c}^{-0.5}\mathrm{Re}_\mathrm{c}^{0.15}$	Transient, Turbulent	0.037	>500%
Haas (1987)	Kenics	$\frac{d_{32}}{D} = 1.2\mathrm{We}_\mathrm{c}^{-0.65}\mathrm{Re}_\mathrm{c}^{-0.2}\left(\frac{\mu_\mathrm{d}}{\mu_\mathrm{c}}\right)^{0.5}$	Laminar, Transient, Turbulent	2.425	14%
Legrand et al. (2001)	SMX	$\frac{d_{32}}{d_\mathrm{p}} = 0.29\mathrm{We}_\mathrm{p}^{-0.2}\mathrm{Re}_\mathrm{p}^{-0.16}$	Laminar, Transient, Turbulent	1.120	3%
Das et al. (2005)	SMX	$\frac{d_\mathrm{max}}{d_\mathrm{p}} = 0.33\mathrm{We}_\mathrm{p}^{-0.33}$	Transient	1.369	15%

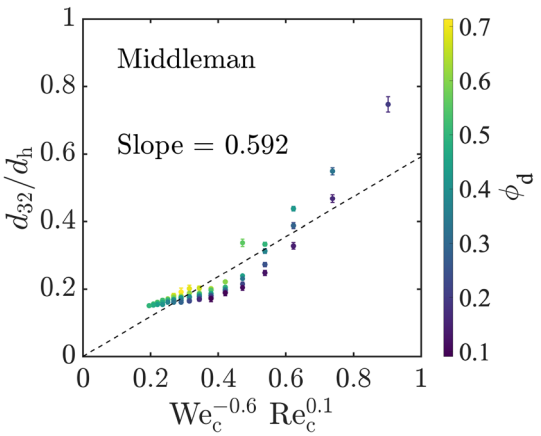


Fig. 15 Ratio of the Sauter mean diameter of droplets to the hydraulic diameter of the micro-mixing units, d_{32}/d_h, as a function of the Weber, We_c, and Reynolds, Re_c, numbers based on the Middleman correlation for the Hinze-Kolmogorov theory of turbulence

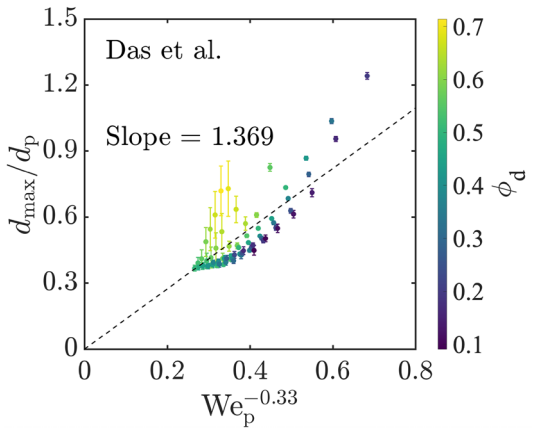


Fig. 16 Ratio of the maximum droplet diameter to the pore diameter in the case of a flow through porous media, $d_\mathrm{max}/d_\mathrm{p}$, as a function of the Weber number, We_p, based on the correlation for the Hinze-Kolmogorov theory of turbulence suggested by Das et al. (2005)

$$\mathrm{We}_\mathrm{p} = \frac{\rho_\mathrm{e} d_\mathrm{p} u_\mathrm{tot}^2}{\sigma}, \tag{17}$$

where the subscript p denotes relation to porous media, the density of emulsion/dispersion, ρ_e, is given by:

$$\rho_\mathrm{e} = \phi_\mathrm{d}\rho_\mathrm{d} + (1-\phi_\mathrm{d})\rho_\mathrm{c}, \tag{18}$$

shifting the range of the observed Reynolds numbers to $266 - 1,163$. In the correlations listed in Table 2, the characteristic channel diameter, D, and the one of the pore, d_p, can be assumed to be equivalent to the hydraulic diameter of the micro-mixing units at the contraction point, d_h.

The proportionality constant K used in the Middleman correlation (see Table 2) was determined in this study by the slope of the linear fit in Fig. 15, with 16.0% RMSE of the observed data to the model. The correlation for an SMV static mixer introduced by Streiff et al. (1997) showed a high degree of error and, therefore, omitted here. Despite deviations from the prior observed values of the proportionality constant, K, the other three correlations developed specifically for laminar and/or transient flow conditions by Haas (1987), Legrand et al. (2001) and Das et al. (2005) showed an improved fit with reduced RMSE. The correlations by Haas (1987) and Legrand et al. (2001) approximated our data points similarly to that by Middleman. However, the fit by Das et al. (2005) revealed a greater tendency to discriminate data points with low droplet size distribution uniformity (see Fig. 16), which is also evidenced by Δ_S in Fig. 9.

Finally, it is worth noting that, although the breakup of liquid interfaces and the formation of dispersion were initially described by the Hinze-Kolmogorov theory of turbulence, valid only for developed turbulent flows, there are alternative dimensionless models for this type of two-phase flow based on the same principles. Some of them were demonstrated to be applicable in describing dispersion formation under laminar and transient flow conditions influenced by secondary flows and vortices/eddies induced within the 'heart/spade' units of static micro-mixers.

4 Conclusions

Hydrodynamic characterisation of the two-phase flow inside the 'heart/spade' units of a micro-mixing plate with a hydraulic diameter of ~ 0.36 mm at the contraction point was studied using an LED-induced fluorescence imaging technique supplemented with CFD simulations.

Experiments were performed using two immiscible fluids: MTBE seeded with Pyrromethane-567 fluorescent dye and deionised water. The droplet size distribution analysis was conducted for a broad range of the dispersed phase (water) ratios, ϕ_{d}, from 0.091 to 0.714. The recorded instantaneous images were qualitatively interpreted to develop a regime map featuring flow patterns: parallel, slugs, and droplets, along with their respective transitional states. An instantaneous image sequence for the droplet size analysis was post-processed using an in-house developed MATLAB-based image processing code to obtain a cumulative probability distribution of droplet diameters.

Following this, a statistical analysis of the resulting droplet diameters was performed to obtain corresponding histograms and to understand the dependence of the Sauter mean diameter of droplets, d_{32}, and the distribution span under various flow conditions. The vortex-induced breakup of the droplet interfaces at increased flow rates was identified to be likely the key mechanism leading to the overall reduction of droplet sizes in the Reynolds number range of $250 - 1,000$. The reduction in the droplet size resulted in a maximum $\sim$ 14-fold increase of the specific surface area, a, for the considered range of flow conditions. The obtained values of d_{32} were empirically correlated with different dimensionless models based on the Hinze-Kolmogorov theory of turbulence. Improved fitting was achieved with alternative correlations derived specifically for laminar and transient flows by Haas (1987), Legrand et al. (2001) and Das et al. (2005), with the latter found to be more discriminative towards higher droplet size distribution spans.

Appendix: Hinze-Kolmogorov energy dissipation model

The Hinze-Kolmogorov theory of turbulence enables the prediction of the maximum droplet diameter, $d_{\max}$, as an equilibrium of the turbulent pressure stresses and the surface tension, defined through the droplet Weber number:

$$\mathrm{We}_{\mathrm{d}} = \frac{\rho_{\mathrm{d}} \overline{\delta u^2(d)} d}{\sigma} \tag{19}$$

where $\overline{\delta u^2(d)}$ represents the two-point spatial autocorrelation of the longitudinal (streamwise) component of fluctuating velocity at a distance d equal to the drop diameter. Within the inertial field of isotropic turbulence, $\overline{\delta u^2(d)}$ was expressed by Batchelor (1953) through the Kolmogorov constant, C_{K}, as:

$$\overline{\delta u^2(d)} = C_{\mathrm{K}} \varepsilon^{2/3} d^{2/3} \tag{20}$$

Droplet breakup takes place as the Weber number reaches its critical value, $\mathrm{We}_{\mathrm{cr}}$ (Lemenand et al. 2013). The maximum diameter of a droplet that can resist the breakup by turbulent forces can be obtained by combining Eqs. 19 and 20 and rearranging them for the droplet diameter:

$$d_{\max} = \left(\frac{\mathrm{We}_{\mathrm{cr}}}{C_{\mathrm{K}}}\right)^{0.6} \left(\frac{\sigma}{\rho_{\mathrm{c}}}\right)^{0.6} \varepsilon^{-0.4} = K \left(\frac{\sigma}{\rho_{\mathrm{c}}}\right)^{0.6} \varepsilon^{-0.4} \tag{21}$$

Acknowledgements The lead author would like to thank the Department of Chemical Engineering at Imperial College London for departmental bursary funding and BASF SE for PhD studentship industrial funding. For validating and affirming our scientific findings, gratitude is extended to Dr Mark Winter, Dr Sophie Vallon and Dr Mengxue Zhang from Corning SAS Reactor Technologies. L.K. and O.K.M. acknowledge the Engineering and Physical Sciences Research Council, United Kingdom, through the EPSRC MEMPHIS (EP/K003976/1) and PREMIERE (EP/T000414/1) Programme Grants. O.K.M. also acknowledges funding from PETRONAS and the Royal Academy of Engineering for a Research Chair in Multiphase Fluid Dynamics. We would like to give thanks to Mr Gavin Barnes in the mechanical workshop at the Department of Chemical Engineering for the CNC milling, surface polish and build of the 'heart/spade' micro-mixing reactor. For the purpose of Open Access, the authors have applied a CC BY public copyright license to any Author Accepted Manuscript version arising from this submission.

Author Contributions F.H.G. is the originator of the research work and the introductory literature review, established design and build of the experimental setup, wrote the main manuscript, performed main mathematical analysis. S.N. worked on the implementation of the high-speed camera and fluorescent analytical equipment, provided MATLAB analysis and support writing of the manuscript. K.S.N. provided support on the implementation of the analytical equipment and supported subsequent analysis in MATLAB. L.K. worked on Computation Fluid Dynamics simulation of the flow patterns backing up experimental observations, written up Experiment and simulation section on the Numerical method. C.H. provided supervision and support on the main research work and the design of the experimental setup. E.J.C.D. provided supervision and support on the main research work and the design of the experimental setup. O.K.M. provided supervision and support on the implementation of the analytical equipment and MATLAB analysis. C.N.M. provided supervision and support on the Computation Fluid Dynamics simulation and interpretation of the observed phenomena. K.H. provided supervision and support on the main research work, design and build of the experimental setup, and mathematical analysis.

Data Availability All of the data for this study were generated in-house and analysed by the authors.

Declarations

Competing interests The authors declare no competing interests.

Open Access This article is licensed under a Creative Commons Attribution 4.0 International License, which permits use, sharing, adaptation, distribution and reproduction in any medium or format, as long as you give appropriate credit to the original author(s) and the source, provide a link to the Creative Commons licence, and indicate if changes were made. The images or other third party material in this article are included in the article's Creative Commons licence, unless

indicated otherwise in a credit line to the material. If material is not included in the article's Creative Commons licence and your intended use is not permitted by statutory regulation or exceeds the permitted use, you will need to obtain permission directly from the copyright holder. To view a copy of this licence, visit http://creativecommons.org/licenses/by/4.0/.

References

Al Taweel AM, Walker LD (1983) Liquid dispersion in static in-line mixers. Canadian J Chem Eng 61(4):527–533. https://doi.org/10.1002/cjce.5450610406

Batchelor GK (1953) The theory of homogeneous turbulence. Cambridge University Press

Bird RB, Stewart W, Lightfoot E (1960) Transport Phenomena, 2nd edn. John Wiley & Sons, New York

Chorin AJ (1968) Numerical solution of the Navier–Stokes equations. Math Comput 22(104):745–745

Corning (2016) Adanced-Flow^{TM} Reactors (AFR). https://www.corning.com/media/worldwide/Innovation/documents/LF_WEB.pdfwww.corning.com

Das P, Legrand J, Moranc-ais P, Carnelle G (2005) Drop breakage model in static mixers at low and intermediate Reynolds number. Chem Eng Sci 60:231–238

Ehrfeld (2022) FlowPlate® Superlative technology. https://www.ehrfeld.com/en/flowplate. www.ehrfeld.com

Haas P (1987) Turbulent dispersion of aqueous drops in organic liquid. AIChE J 33(6):987–995

Harlow FH, Welch JE (1965) Gear method for solving differential equations of gear systems. Phys Fluids 8(12):2182–2189

Hartman RL, McMullen JP, Jensen KF (2011) Deciding whether to go with the flow: evaluating the merits of flow reactors for synthesis. Angew Chem Int Ed 50(33):7502–7519. https://doi.org/10.1002/anie.201004637

Hessel V, Kralisch D, Kockmann N, Noël T, Wang Q (2013) Novel process windows for enabling, accelerating, and uplifting flow chemistry. ChemSusChem 6(5):746–789. https://doi.org/10.1002/cssc.201200766

Hinze JO (1955) Fundamentals of the hydrodynamic mechanism of splitting in dispersion processes. AIChE J 1(3):289–295. https://doi.org/10.1002/aic.690010303

Hirschberg S, Koubek R, Moser F, Schöck J (2009) An improvement of the Sulzer SMX™ static mixer significantly reducing the pressure drop. Chem Eng Res Design 87:524–532. https://doi.org/10.1016/j.cherd.2008.12.021

Ibarra R, Zadrazil I, Matar O, Markides C, Hewitt G (2018) Dynamics of liquid–liquid flows in horizontal pipes using simultaneous two–line planar laser–induced fluorescence and particle velocimetry. Int J Multiph Flow 101:47–63. https://doi.org/10.1016/j.ijmultiphaseflow.2017.12.018

Kahouadji L, Nowak E, Kovalchuk N, Chergui J, Juric D, Shin S, Simmons MJH, Craster RV, Matar OK (2018) Simulation of immiscible liquid–liquid flows in complex microchannel geometries using a front-tracking scheme. Microfluid Nanofluid 22:126. https://doi.org/10.1007/s10404-018-2149-y

Kalli M, Pico P, Chagot L, Kahouadji L, Shin S, Chergui J, Juric D, Matar OK, Angeli P (2023) Effect of surfactants during drop formation in a microfluidic channel: a combined experimental and computational fluid dynamics approach. J Fluid Mech 961:A15. https://doi.org/10.1017/jfm.2023.213

Kolmogorov A (1949) On the breakage of drops in a turbulent flow. Dokl Akad Nauk SSSR 66:825–828. https://doi.org/10.1007/978-94-011-3030-1_50

Legrand J, Morancais P, Carnelle J (2001) Liquid–liquid dispersion in a smx-sulzer static mixer. Institution Chemical Engineers 79:949–956

Lemenand T, Della Valle D, Zellouf Y, Peerhossaini H (2003) Droplets formation in turbulent mixing of two immiscible fluids in a new type of static mixer. Int J Multiph Flow 29(5):813–840. https://doi.org/10.1016/S0301-9322(03)00032-6

Lemenand T, Dupont P, Valle DD, Peerhossaini H (2013) Comparative efficiency of shear, elongation and turbulent droplet breakup mechanisms: review and application. Chem Eng Res Des 91(12):2587–2600. https://doi.org/10.1016/j.cherd.2013.03.017

Lobry E, Theron F, Gourdon C, Le Sauze N, Xuereb C, Lasuye T (2011) Turbulent liquid-liquid dispersion in smv static mixer at high dispersed phase concentration. Chem Eng Sci 66(23):5762–5774. https://doi.org/10.1016/j.ces.2011.06.073

Malet-Sanz L, Susanne F (2012) Continuous flow synthesis. A pharma perspective. J Med Chem 55(9):4062–4098. https://doi.org/10.1021/jm2006029

Mason BP, Price KE, Steinbacher JL, Bogdan AR, McQuade DT (2007) Greener approaches to organic synthesis using microreactor technology. Chem Rev 107(6):2300–2318. https://doi.org/10.1021/cr050944c

Matsumura K, Morishima Y, Masuda K, Ikenaga H (1981) Some performance data of the hi-mixer-an in-line mixer. Chem Ing Tech 53(1):51–52

Middleman S (1974) Drop size distributions produced by turbulent pipe flow of immiscible fluids through a static mixer. Industrial Engineering Chem Process Design Development 13(1):78–83. https://doi.org/10.1021/i260049a015

Markides MCRG, Zadrazil I, Hewitt G (2013) Characteristics of horizontal liquid–liquid flows in a circular pipe using simultaneous high-speed laser-induced fluorescence and particle velocimetry. Int J Multiph Flow 49:99–118. https://doi.org/10.1016/j.ijmultiphaseflow.2012.09.004

Otsu N (1979) A threshold selection method from gray-level histograms. IEEE Trans Syst Man Cybern 9(1):62–66. https://doi.org/10.1109/TSMC.1979.4310076

Pastre JC, Browne DL, Ley SV (2013) Flow chemistry syntheses of natural products. Chem Soc Rev 42(23):8849–8869. https://doi.org/10.1039/C3CS60246J

Plouffe P, Macchi A, Roberge DM (2014) From batch to continuous chemical synthesis-a toolbox approach. Org Process Res Dev 18(11):1286–1294. https://doi.org/10.1021/op5001918

Plouffe P, Bittel M, Sieber J, Roberge DM, Macchi A (2016) On the scale-up of micro-reactors for liquid-liquid reactions. Chem Eng Sci 143:216–225. https://doi.org/10.1016/j.ces.2015.12.009

Plouffe P, Roberge DM, Macchi A (2016) Liquid-liquid flow regimes and mass transfer in various micro-reactors. Chem Eng J 300:9–19. https://doi.org/10.1016/j.cej.2016.04.072

Plouffe P, Roberge DM, Sieber J, Bittel M, Macchi A (2016) Liquid-liquid mass transfer in a serpentine micro-reactor using various solvents. Chem Eng J 285:605–615. https://doi.org/10.1016/j.cej.2015.09.115

Shin S, Chergui J, Juric D (2017) A solver for massively parallel direct numerical simulation of three-dimensional multiphase flows. J Mech Sci Technol 32(4):1739–1751

Shin S, Chergui J, Juric D, Juric D, Matar OK, Craster RV (2018) A hybrid interface tracking – level set technique for multiphase flow with soluble surfactant. J Comput Phys 359:409–435

Streiff FA, Mathys P, Fischer TU (1997) New fundamentals for liquid-liquid dispersion using static mixers. Récents Progrès en Génie des Procédés 11(51):307–314

Theron F, Sauze NL (2011) Comparison between three static mixers for emulsification in turbulent flow. Int J Multiph Flow 37:488–500. https://doi.org/10.1016/j.ijmultiphaseflow.2011.01.004

Theron F, Sauze N, Ricard A (2010) Turbulent liquid-liquid dispersion in Sulzer SMX mixer. Ind Eng Chem Res 49(2):623–632. https://doi.org/10.1021/ie900090d

Wang YX, Wen JM (2006) Gear method for solving differential equations of gear systems. J Phys Conf Ser 48:143–148

Wright S, Zadrazil I, Markides C (2017) A review of solid-fluid selection options for optical-based measurements in single-phase liquid, two-phase liquid–liquid and multiphase solid–liquid flows. Exp Fluids 58:108. https://doi.org/10.1007/s00348-017-2386-y

Yamamoto T, Kawasaki H, Kumazawa H (2007) Relationship between the dispersed droplet diameter and the mean power input for emulsification in three different types of motionless mixers. J Chem Eng Jpn 40(8):673–678. https://doi.org/10.1252/jcej.40.673

Publisher's Note Springer Nature remains neutral with regard to jurisdictional claims in published maps and institutional affiliations.